ORIGINAL PAPER

Deposition of nano-crystalline tungsten carbide powders from gaseous WO$_2$(OH)$_2$
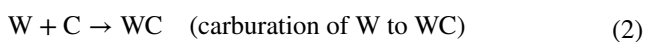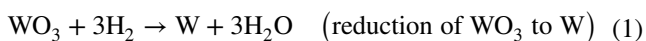
Markus Ostermann[1] · **Roland Haubner**[1]

Abstract

Lower WC grain sizes in the nanometer range have positive effects on the properties of hardmetals (e.g., hardness), but the established production processes of WC are limited to grain sizes of about 150 nm. To produce WC powder with grain sizes in the lower nanometer range, an alternative WC production process based on the chemical vapor transport (CVT) reaction of WO$_3$ and H$_2$O forming gaseous WO$_2$(OH)$_2$ at about 1100 °C, followed by a carburation reaction with H$_2$/CH$_4$-gas mixtures was investigated. The influences of different process parameters such as furnace temperature, humidity and gas flows were investigated to improve the process. With the right set of parameters the produced powder consisted mainly of agglomerated WC grains with a size of about 5 nm. Beside the common hexagonal WC phase, the cubic WC$_{1-x}$ phase was stabilized due to the small crystallite sizes. In addition, a thin layer of amorphous carbon was present on the powder surface due to the catalytic methane decomposition on the WC surface. The amount of oxidic and metallic residues in the product powder was minimized with the parameter optimization and the powder yield was increased up to about 50%. With further optimization of the process parameters and usage of improved flow breakers, the purity and yield of the product powder can be further improved. Since an application in the hardmetal section is not realistic at the moment, applications in the catalysis sector could be considered due to the small grain size and good catalytic activity of the cubic WC$_{1-x}$ phase.

Keywords Tungsten carbide · CVT-mechanism · WO$_2$(OH)$_2$ · Carburation · Nano-sized powder · Transmission electron microscopy (TEM)

1 Introduction

The industrial well-established WC powder production process is a two-step process. Tungsten oxide powder is reduced in push-type or rotary furnaces with hydrogen to produce tungsten powder (Eq. 1), which is carburized afterwards with carbon black mainly in push-type furnaces (Eq. 2). Both reactions have been well studied and described in literature [1–6]:

$$WO_3 + 3H_2 \rightarrow W + 3H_2O \quad (\text{reduction of WO}_3 \text{ to W}) \quad (1)$$

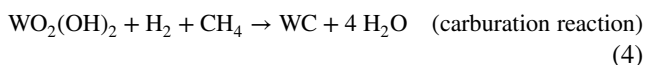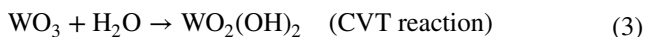$$W + C \rightarrow WC \quad (\text{carburation of W to WC}) \quad (2)$$

This process is limited at grain sizes of about 150 nm. Smaller grain sizes may enhance the properties (e.g., hardness) of a further produced WC–Co-hardmetal [7], but to achieve these grain sizes below 100 nm, alternative processes are necessary.

The approach of this study to reach small grain sizes, is to produce a gaseous tungsten species and to carburize it in the gas phase. An earlier described process using WCl$_6$ as precursor was not successful [8]; another easier to handle and in literature described [9–12] way to generate a gaseous tungsten species is the chemical vapour transport (CVT) reaction of WO$_3$ with H$_2$O (Eq. 3) resulting in gaseous WO$_2$(OH)$_2$. This hydroxide is transported from the evaporation site and brought in contact with a H$_2$/CH$_4$-reaction gas mixture to obtain WC deposition from the gas phase (Eq. 4). Due to the high nucleation rate in the gas phase the crystal size of the deposited WC should be in the lower nanometer range. Furthermore, it would be a one-step process from the WO$_3$ educt to WC in contrast to the established industrial process [1]:

✉ Roland Haubner
  roland.haubner@tuwien.ac.at

1 TU Wien, Institute of Chemical Technologies and Analytics, Getreidemarkt 9/164-03, 1060 Vienna, Austria

$$WO_3 + H_2O \rightarrow WO_2(OH)_2 \quad \text{(CVT reaction)} \qquad (3)$$

$$WO_2(OH)_2 + H_2 + CH_4 \rightarrow WC + 4\,H_2O \quad \text{(carburation reaction)} \qquad (4)$$
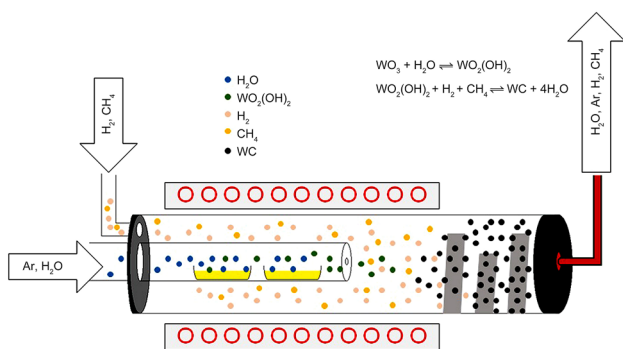
In addition, the influence of different process parameters such as furnace temperature, humidity and gas flows (argon, hydrogen, methane) on the evaporation process, the product yield and the product composition was investigated.

2 Experimental procedure

In Fig. 1, the experimental equipment is illustrated. It was modified after experiments for the production of fine W powders [10]. Two externally heated quartz tubes were arranged concentrically. The inner small tube was connected with the outer big tube by a small hole at the end of the inner tube. The system was conductively heated by a Kanthal furnace surrounding the quartz tubes.

Two quartz boats, filled with about 7.5 g of a WO$_3$ powder each, were placed in the inner tube. After reaching the process temperature humid Ar was passed over the WO$_3$ to generate the gaseous WO$_2$(OH)$_2$. The humidity of the Ar-flow was adjusted via the vapor pressure of the water by passing the gas through a thermostated bubbler filled with deionized water [11].

Fig. 1 Scheme of the setup used for the production of the nanometer-sized WC powder

The amount of evaporated WO$_3$ was determined by means of differential weighing of the powder used, before and after the respective test.

The generated WO$_2$(OH)$_2$ was transported by the Ar flow through the small hole to the outer quartz tube, where it got in contact with the H$_2$/CH$_4$-reaction gas and spontaneously reacted to WC. The collection of the product powder occurred at the end of the outer quartz tube, where tungsten platelets were used as flow breakers in most of the experiments.

X-ray diffraction (XRD), scanning electron microscopy (SEM), transmission electron microscopy (TEM) and Raman spectroscopy were used to characterize the product.
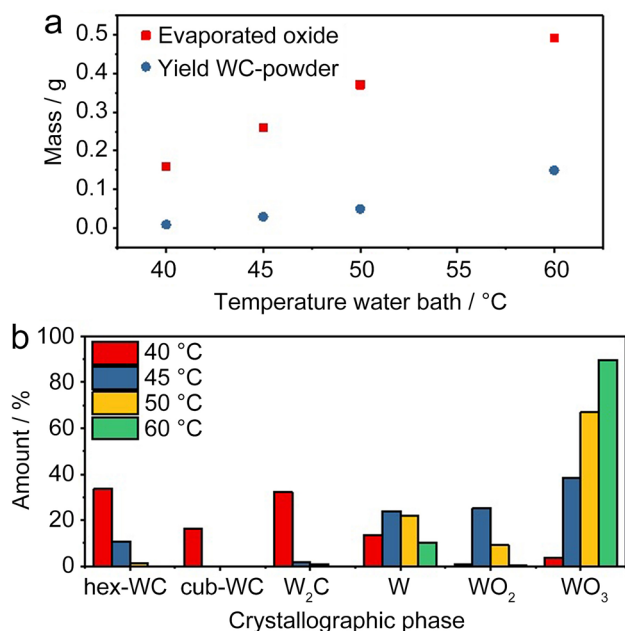
3 Results and discussion

The results of the variation of the water bath temperature, furnace temperature and the methane gas flow are described in this paper. The variation of the other gas flows (Ar, H$_2$), process duration and the influence of the flow breakers are described in the diploma thesis of Ostermann [11].

3.1 Variation of the temperature of the water bath

The water bath temperature was varied in the range of 40–60 °C, and therefore, the humidity of the argon gas was in the range of 7.29–19.67%. The other parameters were fixed according to Table 1.

Figure 2a shows the mass of the evaporated oxide and deposited powder at different water bath temperatures. With increasing humidity the transport is also increasing, due to the shift of the reaction equilibrium towards the hydroxide WO$_2$(OH)$_2$, leading to higher evaporation and deposition rates.

Via XRD and Rietveld analysis the composition of the product powders at different water bath temperatures was determined (Fig. 2b). With increasing humidity the amount of oxidic residues is simultaneously increasing. At a water bath temperature of 50 °C (12.2% humidity) small amounts of carbidic phases are observable, whereas at 40 °C (7.3% humidity) the carbidic phases are the dominating phases in

Table 1 Fixed parameters during the variation of the temperature of the water bath, furnace temperature and CH$_4$-gas flow

	Temperature water bath	Furnace temperature	CH$_4$-gas flow
Temperature water bath (°C)	Variable	45	45
Furnace temperature (°C)	1100	Variable	1100
Ar-gas flow (mL·min^{-1})	1000	1000	1000
H$_2$-gas flow (mL·min^{-1})	1000	1000	1000
CH$_4$-gas flow (mL·min^{-1})	250	300	Variable
Duration (h)	2	2	2

Fig. 2 Variation of the water bath temperature: **a** mass of the evaporated oxide powder and product powder; **b** composition of the product powder according to XRD and Rietveld analysis ($T_{furnace}$ 1100 °C; 1000 mL·min^{-1} Ar; 1000 mL·min^{-1} H$_2$, 250 mL·min^{-1} CH$_4$; 2 h)

the powder and only small amounts of oxidic residues are left. This is due to the positive effect of a lower humidity on the carburation reaction, which results in a shift of the reaction equilibrium (Eq. 4) to the product side. However, because a lower humidity is unfavorable for the transport process and, therefore, results in a very low evaporation rate and powder yield, 45 °C water bath temperature (9.5% humidity) was chosen to proceed in an attempt to balance the transport and the carburation process.

The powder produced at 40 °C was analyzed using TEM and electron diffraction (Fig. 3). Figure 3a shows an overview of the powder. It is agglomerated and consists mainly of three different crystallite shapes. There are bigger grains with a size of about 100 nm, smaller grains with a size of about 25 nm and rod-shaped crystallites with a size of about 80 nm. The electron diffraction (Fig. 3b) pattern shows that the area contains the tungsten carbide phases hex-WC and cub-WC$_{1-x}$, which are the most intense phases, but also residues of the metallic tungsten phase and the oxidic WO$_3$ phase are observable. Figure 3c shows an area with grains with a size of about 25 nm. According to the electron diffraction pattern of this area (Fig. 3d), these grains consist mainly of the cubic WC$_{1-x}$ phase. Figure 3e shows an area dominated by the rod-shaped crystallites. These consist mainly
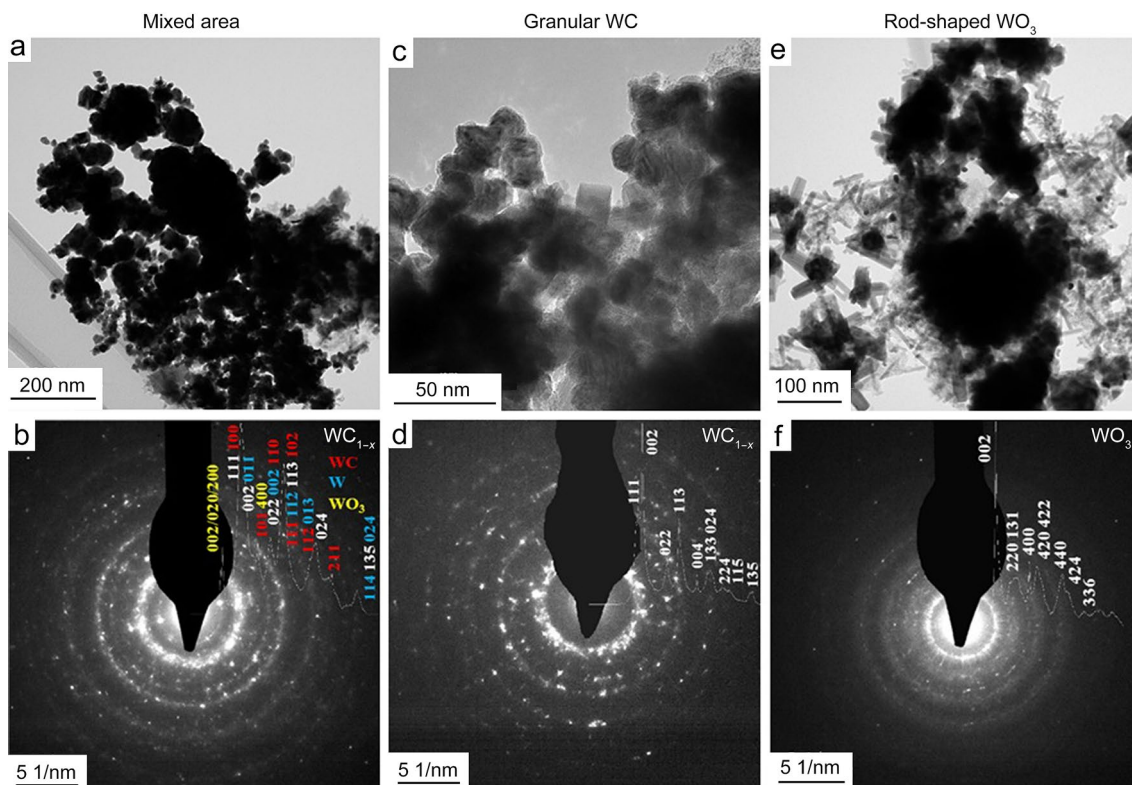
Fig. 3 TEM micrographs (**a**, **c**, **e**) and electron diffraction patterns (**b**, **d**, **f**) of different parts of the sample produced at 40 °C water bath temperature. **a**, **b** mixed area, **c**, **d** granular WC, **e**, **f** rod-shaped WO$_3$. ($T_{furnace}$ 1100 °C; 1000 mL·min^{-1} Ar; 1000 mL·min^{-1} H$_2$, 250 mL·min^{-1} CH$_4$; 2 h)

of the oxidic WO$_3$ phase according to the electron diffraction pattern (Fig. 3f). The rod shape could be a result of the deposition conditions due to a deposition process similar to the whisker growth of the WO$_{2.72}$-needles at the reduction of WO$_3$ [2–4]. The start of the deposition could be a WO$_3$ particle out of the gas phase on whom further oxidic species deposit to form these rod-shaped structures. The reduction and carburation process do not take place due to the insufficient dwelling time of these particles in the hotter areas of the furnace. Therefore, different deposition conditions are observable due to the temperature gradient at the end of the outer quartz tube, leading to oxidic and metallic residues beside the desired carbide phases in the product powder.

3.2 Variation of the furnace temperature

The furnace temperature was varied between 1000 and 1125 °C, whereas the other parameters were fixed according to Table 1. In Fig. 4a, the mass of the evaporated oxide and the deposited product powder at different furnace temperatures is shown. With increasing temperature, the evaporation rate and consequently the deposition rate are increasing. This increase of the evaporation rate is due to the shift of the reaction equilibrium steadily to the side of the hydroxide.

Via XRD and Rietveld analysis the product powder composition at different furnace temperatures was calculated according to Fig. 4b. Under 1100 °C the powder consists
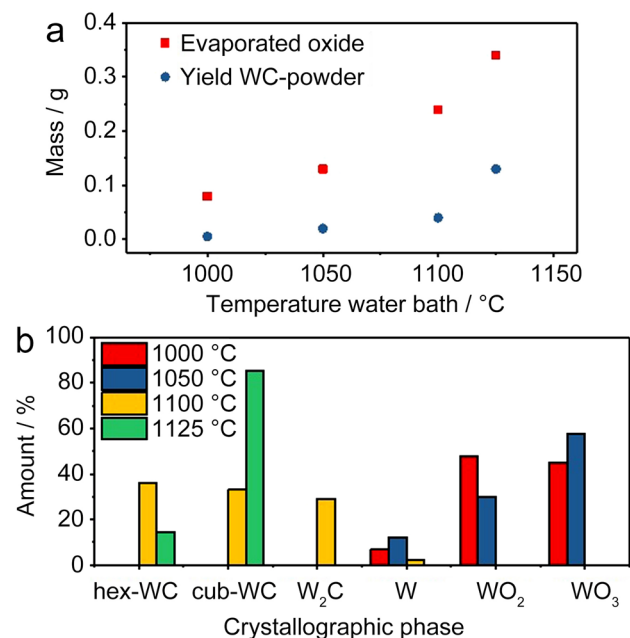
Fig. 4 Variation of furnace temperature: **a** mass of the evaporated oxide powder and the product powder produced; **b** composition of the product powder according to XRD and Rietveld analysis. ($T_{water\ bath}$ 45 °C; 1000 mL·min^{-1} Ar; 1000 mL·min^{-1} H$_2$, 300 mL·min^{-1} CH$_4$; 2 h)

mainly of oxidic residues and about 10% of a metallic tungsten phase. The carburation does not take place at temperatures below 1100 °C. At temperatures of 1100 °C upwards no oxidic residues are present in the product powder. At 1100 °C the carburation process is uncompleted with the product powder containing metallic tungsten and W$_2$C, whereas at 1125 °C only the cubic.

WC$_{1-x}$ and the hexagonal WC phases are present in the powder. In general, the amount of carbide phases increases with increasing furnace temperature, due to the positive effect of higher process temperatures on the carburation reaction.

The presence of the cubic WC$_{1-x}$ phase is an indication for grain sizes in the lower nanometer range, because this cubic phase can only be observed at these small grain sizes. The stability of a cubic WC$_{1-x}$ phase at grain sizes below 40 nm was also described in literature by Zavodinsky et al. [12], Abdullaeva et al. [13] and Pak et al. [14].

The powder produced at 1125 °C furnace temperature was analyzed using TEM and electron diffraction measurements (Fig. 5). The TEM micrographs (Fig. 5a–c) show agglomerated structures of smaller grains. The grain sizes are in the single-digit nanometer range at about 5 nm. The electron diffraction pattern (Fig. 5d) was obtained over an area of about 100 nm diameter. The pattern doesn't resemble the pattern of the thermodynamically stable hexagonal WC phase, but resembles the pattern of the cubic WC$_{1-x}$ phase, which is a high temperature modification stabilized by the grain sizes below 40 nm. This corresponds well with the data gained by XRD. The broadened bands could result from amorphous parts in the powder.

3.3 Variation of the CH$_4$-gas flow

The CH$_4$-gas flow was varied between 100 and 600 mL·min^{-1}, whereas the other process parameters were fixed according to Table 1. The mass of the evaporated oxide and the product powder for each CH$_4$-gas flow is shown in Fig. 6a. The evaporation rate remains steady at about 0.25 g evaporated oxide per 2 h process duration at a CH$_4$-gas flow of 100–400 mL·min^{-1}. At 600 mL·min^{-1} the evaporation rate drops to 0.21 g per 2 h, because the small hole on the end of the small tube is increasingly overgrown by carbon black out of the methane decomposition. This hinders more and more the Ar-gas flow and thereby the evaporation and transportation process. The product powder yield is increasing with increasing CH$_4$-gas flow, due to the increasing shift of the carburation reaction (Eq. 4) equilibrium on the product side with increasing CH$_4$-concentration. Another reason for the steady increase of the product powder yield is the increasing decomposition of CH$_4$ to carbon black and H$_2$ with higher CH$_4$-concentration in the reaction gas. At 600 mL·min^{-1} CH$_4$-gas flow the methane decomposition

Fig. 5 TEM micrographs (**a–c**) and electron diffraction pattern (**d**) of the product powder produced at 1125 °C ($T_{\text{water bath}}$ 45 °C; 1000 mL·min^{-1} Ar; 1000 mL·min^{-1} H$_2$, 300 mL·min^{-1} CH$_4$; 2 h)
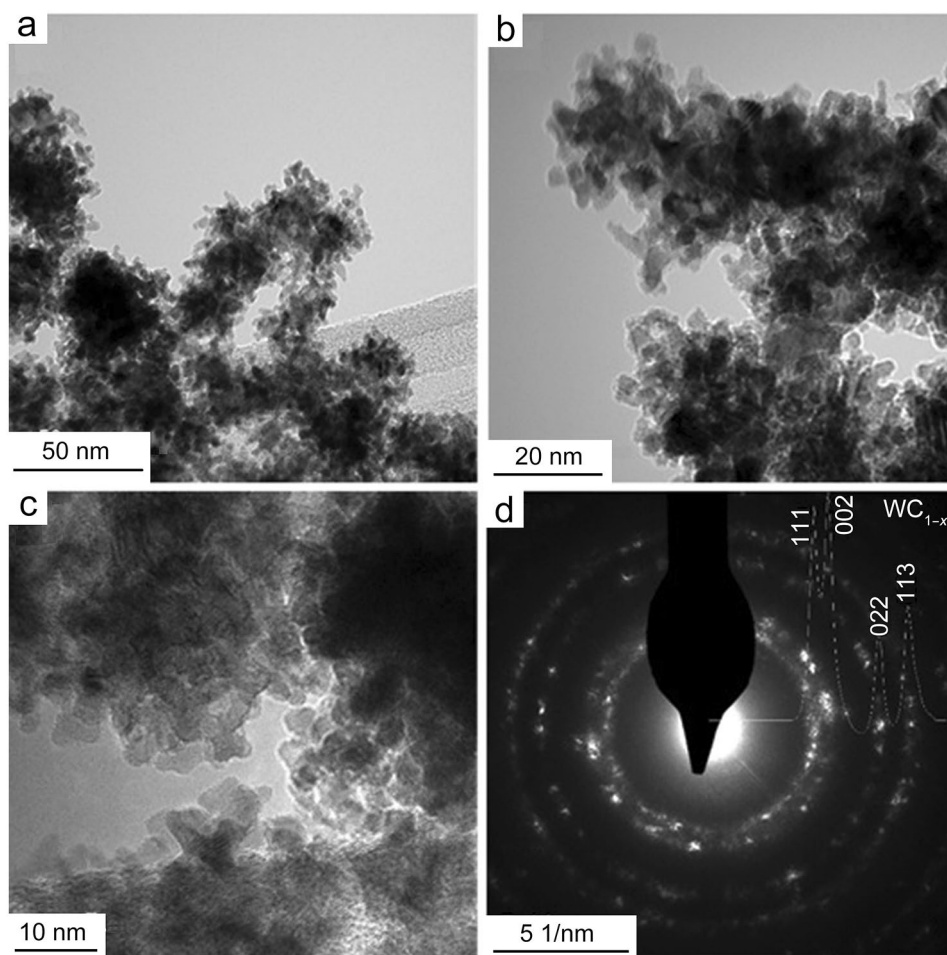
dominates the process leading to a higher mass of the product powder than that of the evaporated oxide.

Via XRD and Rietveld analysis the composition of the product powder at different CH$_4$-gas flows was calculated. In Fig. 7, the XRD diffractograms are shown, and in Fig. 6b, the calculated amounts of each observed phase. At low gas flows of 250 mL·min^{-1} and below, large amounts of oxidic residues and metallic tungsten are present. The amount of carbidic tungsten phases is at about 15%. At 300 mL·min^{-1} the amount of oxidic and metallic tungsten phases drops to 2% and thereby the amount of the carbidic phases increases simultaneously with the amount of each of the carbidic phase (W$_2$C, cub-WC$_{1-x}$, hex-WC) at about 30%. By increasing the CH$_4$-gas flow to 400 mL·min^{-1}, the amount of the residues drops further to about 1%. The carburation becomes more completed due to the amount of the higher carbidic phases (cub-WC$_{1-x}$, hex-WC) increasing to 72% in contrast to 62% at 300 mL·min^{-1}. The amount of the ditungsten carbide is decreasing simultaneously. In contrast to the positive trend of the increase of the CH$_4$ concentration on the process, the product powder consists mainly of carbon black and graphite with oxidic residues at 600 mL·min^{-1} CH$_4$-gas flow. A reduction or carburation process is not observable, due to the dominating methane decomposition at this high CH$_4$ concentration. Therefore, the optimal range for the CH$_4$-gas flow is about 300–400 mL·min^{-1} with a H$_2$-gas flow of 1000 mL·min^{-1}.

In Fig. 8, SEM micrographs of the powders produced at 100 mL·min^{-1}, 250 mL·min^{-1} and 400 mL·min^{-1} CH$_4$-gas flow are shown at two magnifications. The powders heavily resemble each other. They consist of agglomerates up to about 100 µm. At higher magnification a densely branched network of small grains is observable, but the resolution of the SEM is insufficient to observe crystallites and measure their size.

Due to the insufficient resolution of the SEM, it is necessary to use TEM for further characterization. In Fig. 9, TEM micrographs of the same powder samples used in SEM (100 mL·min^{-1}, 250 mL·min^{-1} and 400 mL·min^{-1} CH$_4$-gas flow) are shown.

At 100 mL·min^{-1} CH$_4$-gas flow (Fig. 9a, b) merely rod-shaped crystallites with a size of 30–135 nm are visible. The electron diffraction pattern resembles strongly the
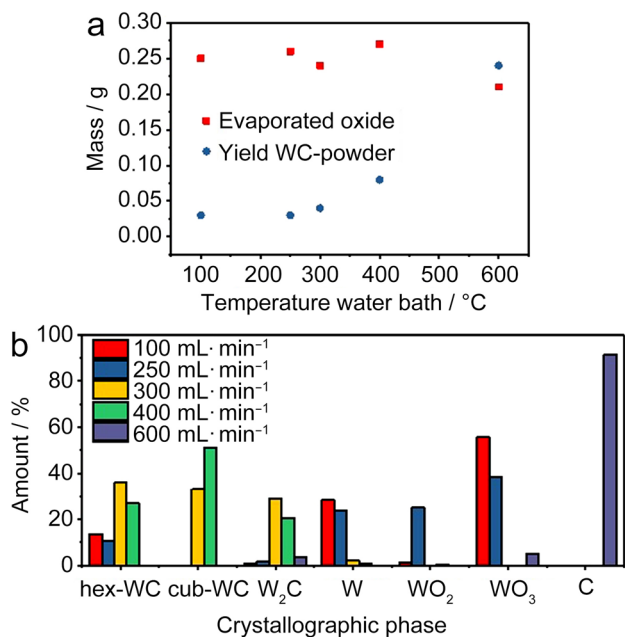
Fig. 6 Variation of the CH_4-gas flow: **a** mass of the evaporated oxide powder and the product powder; **b** composition of the product powders according to XRD and Rietveld analysis. ($T_{water bath}$ 45 °C; $T_{furnace}$ 1100 °C; 1000 mL·min^{-1} Ar; 1000 mL·min^{-1} H$_2$, 2 h)

pattern of WO_3, which is in agreement with the results of the XRD, where also WO_3 is the dominating phase. The crystallites are agglomerated with a common center, which could be a deposition nucleus out of the gas phase on whom the $WO_2(OH)_2$ decomposed to build WO_3 and H_2O.

Reaching 250 mL·min^{-1} CH_4-gas flow (Fig. 9c, d) the rod-shaped crystallites already observed at 100 mL·min^{-1} CH_4-gas flow are still the dominating phase. However, beside these crystallites small grains with a size of about 5 nm are visible.

At 400 mL·min^{-1} CH_4-gas flow (Fig. 9e, f) the dominating morphology of the crystallites changes from the rod-shaped crystallites to small grains with a size in the single-digit nm-range. The crystallites are heavily agglomerated. On the surface of the grains a thin, light layer is visible. This

could be a carbon black layer resulting from the methane decomposition on the surface of the carbide grains. The electron diffraction pattern resembles the pattern of cubic WC_{1-x} with satellites of the hexagonal WC in between (similar to Fig. 5d). These results are in agreement with the XRD measurements. The broadened bands of the diffraction pattern could result of amorphous parts in the powder.

To determine the presence of amorphous carbon in the produced powder Raman spectroscopy was used. Multiple spectra of the powder produced at a CH_4-gas flow of 400 mL·min^{-1} and an industrial WC powder were measured and are shown in Fig. 10. Both powders show four bands below 820 cm^{-1}, which are bands from the WC. The produced WC powder shows in contrast to the industrial powder two additional bands at about 1360 cm^{-1} and 1610 cm^{-1} beside the WC-bands. These are the D- and G-band of carbon. Due to the high intensity of the D-band and the broad structure of the bands, it resembles the band structure of microcrystalline graphite or carbon black [15, 16]. Therefore, the presence of amorphous carbon in the produced powder is very likely.

## 3.4 Reaction mechanism and general discussion

The humidity is in general the essential factor for the transport process and can be controlled by the temperature of the water bath and the Ar-gas flow, whereas increasing humidity increases the evaporation rate. In addition, a higher furnace temperature has a positive effect on the transport reaction, which was already shown by literature [10].

In contrast a higher humidity shows an inhibiting effect on the carburation reaction leading to oxidic phases and only small amounts of carbides in the powder. The crystallites are mainly rod-shaped with a size of about 25–100 nm consisting mainly of WO_3.

At a lower humidity and a furnace temperature of at least 1100 °C the carburation process takes place, leading to grains with a size of about 5 nm. Due to this small crystallite sizes of the carbide grains the high temperature modification cubic WC_{1-x} is stabilized besides the hexagonal WC phase. This stabilizing effect of small crystallite sizes on the cubic

Fig. 7 Variation of the CH_4-gas flow: XRD diffractograms of the product powders ($T_{water bath}$ 45 °C; $T_{furnace}$ 1100 °C; 1000 mL·min^{-1} Ar; 1000 mL·min^{-1} H$_2$, 2 h)
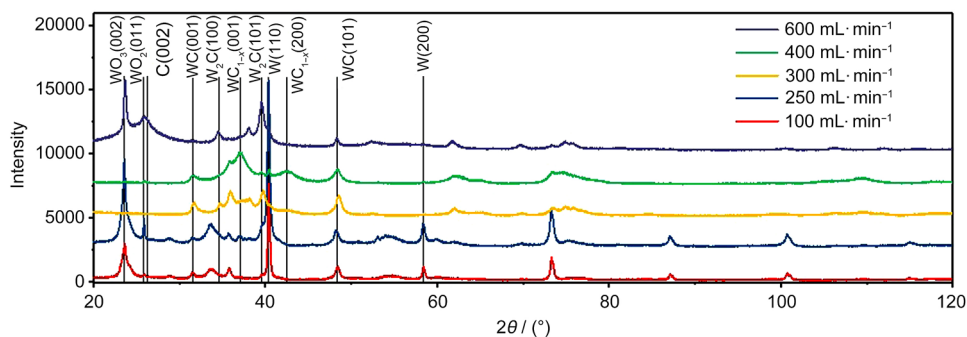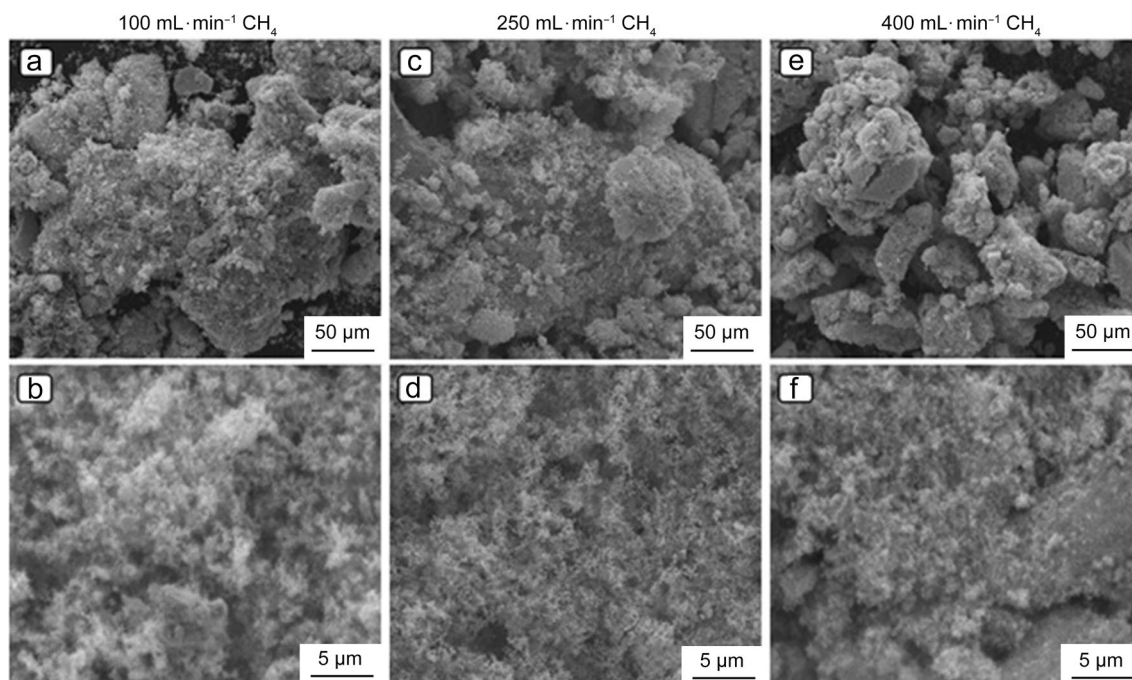
Fig. 8 SEM micrographs of the product powders produced at CH_4-gas flows of **a**, **b** 100 mL·min^{-1}, **c**, **d** 250 mL·min^{-1} and **e**, **f** 400 mL·min^{-1}. ($T_{water\ bath}$ 45 °C; $T_{furnace}$ 1100 °C; 1000 mL·min^{-1} Ar; 1000 mL·min^{-1} H_2, 2 h)
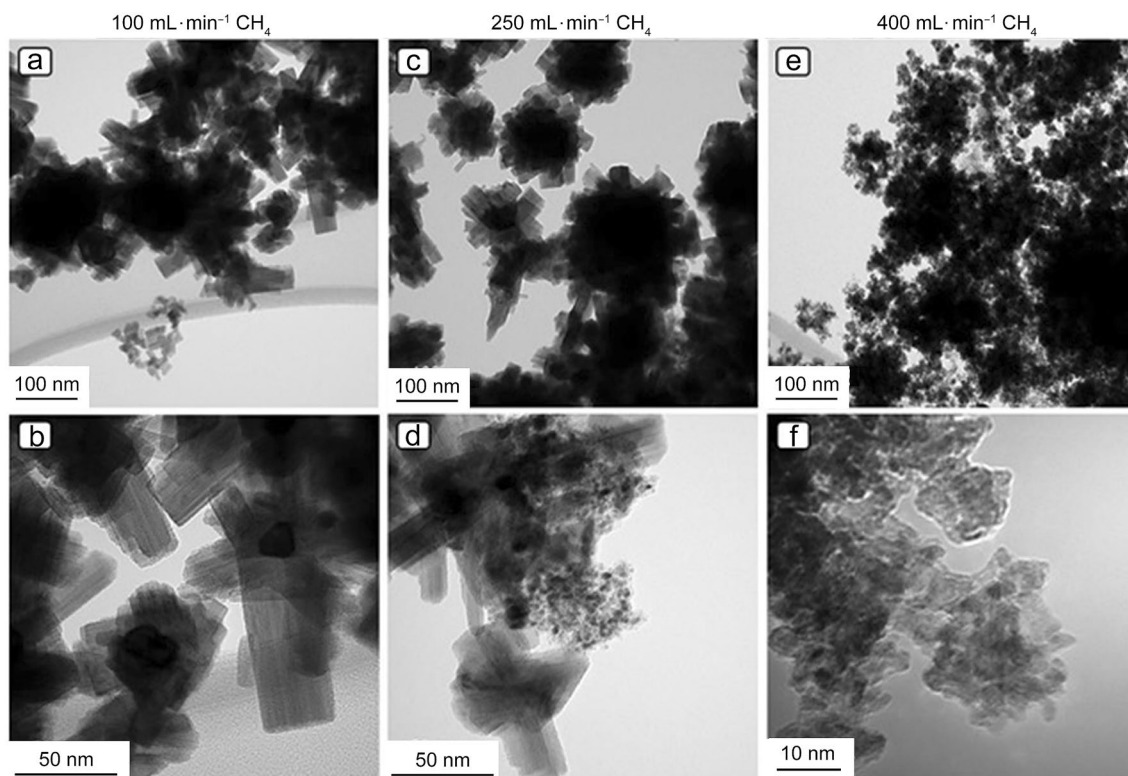
Fig. 9 TEM micrographs and electron diffraction patterns of the product powders produced at CH_4-gas flows of **a**, **b** 100 mL·min^{-1}, **c**, **d** 250 mL·min^{-1} and **e**, **f** 400 mL·min^{-1}. ($T_{water\ bath}$ 45 °C; $T_{furnace}$ 1100 °C; 1000 mL·min^{-1} Ar; 1000 mL·min^{-1} H_2, 2 h)

Fig. 10 Comparison of Raman measurements of **a** WC powder produced by CVT (400 mL·min^{-1} CH_4); **b** industrial WC
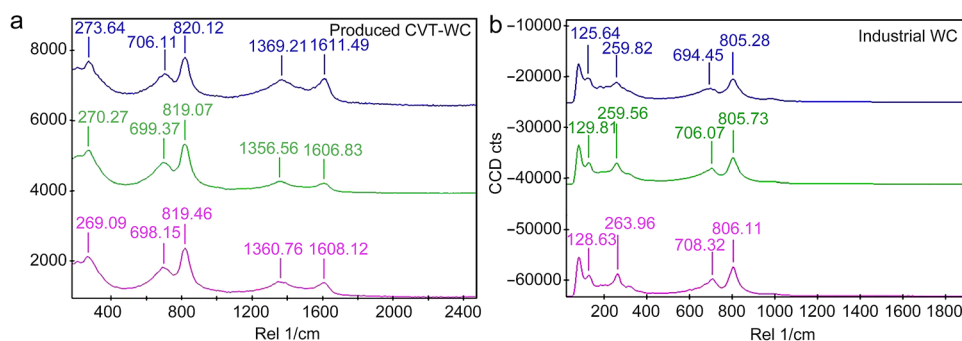
WC_{1-x} phase has already been shown in literature [13–15]. Beside the carburation reaction the decomposition of methane takes place, which is additionally catalyzed by the forming WC. This catalytic effect is also shown in literature [17, 18]. This leads to the formation of amorphous carbon on the surface of the carbide grains hindering further deposition of tungsten species out of the gas phase on the surface and, therefore, hindering grain growth. The surface can be observed using TEM measurements (for example, Fig. 5b) and amorphous carbon is also detectable via the D- and G-band of carbon in Raman spectroscopy. If the methane concentration in the reaction gas is too high, due to a lower H_2-gas flow or a higher CH_4-gas flow, the methane decomposition becomes the main reaction of the system. In this case, the carburation reaction does not take place due to the depletion of methane in the gas phase following the dominating methane decomposition, leading to a product powder mainly consisting of carbon black, graphite and WO_3.

Therefore, balancing the humidity in the way that on the one hand the mass of the transported oxide is maximized and on the other hand the carburation reaction is taking place and not hindered by the humidity, is essential for the process. In addition, the adjustment of the composition of the reaction gas to reach the sweet spot between too little methane to carry out the carburation reaction and too much methane to reach the area, where the methane decomposition overtakes the carburation process, is also of high importance.

4 Summary and outlook

Using this process based on a CVT reaction of WO_3 with H_2O leading to gaseous $WO_2(OH)_2$ and a carburation reaction with a CH_4/H_2-gas mixture, the production of a WC powder with crystallite sizes in the single-digit nanometer range in a one-step process is possible. Due to these small crystallite sizes, the cubic high-temperature modification WC_{1-x} is stabilized beside the hexagonal WC. The surface of the powder is covered by a thin layer of amorphous carbon, which could be hindering grain growth during the production process, but also be a problem regarding

surface applications. By optimizing the process parameters the amount of carbide phases in the product powder (cub-WC_{1-x}, hex WC) was increased to more than 95% and the powder yield was increased to about 50% of the theoretical yield.

Further optimization of the process parameters such as higher furnace temperature and optimizing the flow breakers (e.g., with a combination of grids and platelets) is necessary to improve the process and increase the purity and the powder yield.

Applications in the hardmetal section are at the moment not realistic due to the low throughput and conversion rate. However, applications in the catalysis section, where the use of hexagonal WC but also cubic WC_{1-x} as an alternative for noble metal catalysts is described by literature [18, 19], could be considered, due to the low grain sizes.

Declarations

Conflict of interest The authors declare no conflict of interest.

References

1. Lasner E, Schubert WD. Tungsten: properties, chemistry, technology of the element, alloys, and chemical compounds. New York: Kluwer Academic; 1999.
2. Haubner R, Schubert WD, Lassner E, Schreiner M, Lux B. Mechanical of technical reduction of tungsten: part 1 literature review. Int J Refract Metal Hard Mater. 1983;3:108.
3. Haubner R, Schubert WD, Hellmer H, Lassner E, Lux B. Mechanical of technical reduction of tungsten: part 2 hydrogen reduction of tungsten blue oxide to tungsten powder. Int J Refract Metal Hard Mater. 1983;4:156.
4. Venables DS, Brown ME. Reduction of tungsten oxides with hydrogen and with hydrogen and carbon. Thermochim Acta. 1996;285(2):36.
5. Natter H, Lackner A, Knunz G, Hempelmann R. In situ high temperature X-ray diffraction study on tungsten carbide formation. In: Kneringer G, Rodhammer P, Wildner H (eds) 15th International Plansee seminar, Plansee holding AG, Reutte, vol 2, 2001.
6. Mühlbauer G, Kremser G, Bock A, Weidow J, Schubert W-D. Transition of W_2C to WC during carburization of tungsten metal powder. Int J Refract Metal Hard Mater. 2018;72:141.
7. Schubert WD. Feinst- und Ultrafeinkornhartmetalle—vom Pulver zum Werkzeug. Keram Z. 2015;67(7):365.
8. Tang X, Haubner R, Lux B, Kieffer B. Preparation of ultrafine CVD WC powders deposited from WCl_6 gas mixtures. J Phys IV. 1995;5:1013.
9. Glemser O, Wendlandt HG. Gaseous hydroxides. In: Emeléus HJ, Sharpe AG, editors. Advances in inorganic chemistry and radiochemistry, vol. 5. Elsevier; 1963. p. 215.
10. Ostermann M, Dalbauer V, Schubert WD, Haubner R. Preparation of nano-crystalline tungsten powders from gaseous $WO_2(OH)_2$. Tungsten. 2021;4(1):60.
11. Ostermann M. Production of very fine grained tungsten and tungsten carbide powders with the transport reaction of $WO_2(OH)_2$. Diploma Thesis, Wien; 2019.
12. Zavodinsky VG. Small tungsten carbide nanoparticles: simulation of structure, energetics, and tensile strength. Int J Refract Metal Hard Mater. 2010;28(3):446.
13. Abdullaeva Z, Omurzak E, Iwamoto C, Okudera H, Koinuma M, Takebe S, et al. High temperature stable WC_{1-x}@C and TiC@C core–shell nanoparticles by pulsed plasma in liquid. RSC Adv. 2013;3(2):513.
14. Pak A, Sivkov A, Shanenkov I, Rahmatullin I, Shatrova K. Synthesis of ultrafine cubic tungsten carbide in a discharge plasma jet. Int J Refract Metal Hard Mater. 2015;48:51.
15. Tuinstra F, Koenig JL. Raman spectrum of graphite. J Chem Phys. 1970;53(3):1126.
16. Tamor MA, Vassell WC. Raman '"fingerprinting"' of amorphous carbon films. J Appl Phys. 1994;76(6):3823.
17. Claridge JB, York APE, Brungs AJ, Marquez-Alvarez C, Sloan J, Tsang SC, Green MLH. New catalysts for the conversion of methane to synthesis gas: molybdenum and tungsten carbide. J Catal. 1998;180(1):85.
18. Kim J, Jang JH, Lee YH, Kwon YU. Enhancement of electrocatalytic activity of platinum for hydrogen oxidation reaction by sonochemically synthesized WC_{1-x} nanoparticles. J Power Sources. 2009;193(2):441.
19. Gammer C, Mangler C, Rentenberger C, Karnthaler HP. Quantitative local profile analysis of nanomaterials by electron diffraction. Scripta Mater. 2010;63(3):312.